Nanoscale Res Lett (2009) 4:913–920
DOI 10.1007/s11671-009-9330-x

NANO EXPRESS

# Molecular Dynamics Simulations of the Roller Nanoimprint Process: Adhesion and Other Mechanical Characteristics

**Cheng-Da Wu · Jen-Fin Lin · Te-Hua Fang**

Received: 5 March 2009 / Accepted: 24 April 2009 / Published online: 29 May 2009


**Abstract** Molecular dynamics simulations using tight-binding many body potential are carried out to study the roller imprint process of a gold single crystal. The effect of the roller tooth's taper angle, imprint depth, imprint temperature, and imprint direction on the imprint force, adhesion, stress distribution, and strain are investigated. A two-stage roller imprint process was obtained from an imprint force curve. The two-stage imprint process included the imprint forming with a rapid increase of imprint force and the unloading stage combined with the adhesion stage. The results show that the imprint force and adhesion rapidly increase with decreasing taper angle and increasing imprint depth. The magnitude of the maximum imprint force and the time at which this maximum occurs are proportional to the imprint depth, but independent of the taper angle. In a comparison of the imprint mechanisms with a vertical imprint case, while high stress and strain regions are concentrated below the mold for vertical imprint, they also occur around the mold in the case of roller imprint. The regions were only concentrated on the substrate atoms underneath the mold in vertical imprint. Plastic flow increased with increasing imprint temperature.

**Keywords** Roller imprint · Nanoimprint · Molecular dynamics · Nanotribology · Taper

C.-D. Wu · J.-F. Lin (✉)
Department of Mechanical Engineering and Center for Micro/Nano Science and Technology, National Cheng Kung University, Tainan 701, Taiwan
e-mail: jflin@mail.ncku.edu.tw

T.-H. Fang
Institute of Mechanical and Electromechanical Engineering, National Formosa University, Yunlin 632, Taiwan

## Introduction

With the increasing demand for nano/micropatterns on large substrates, the establishment of large-scale nanofabrication technology has become a priority. In recent years, nanoimprint lithography (NIL) has become a popular method that offers a sub-10 nm feature size, high throughput, and low cost [1, 2]. NIL fabricates nanopatterns by pressing a hard stamp with nanopatterns into a thin film and deforming the film mechanically. A similar approach to flat imprint lithography, roller nanoimprint lithography (RNIL) with a sub-100-nm feature size, was proposed by Chou et al. in 1998 [3].

Roller imprint technology such as gravure offset printing and flexography printing offered an alternative approach to large-scale pattern fabrication [4, 5]. Compared with vertical NIL, RNIL has the advantages of producing better uniformity, requiring less force, and being able to repeat a mask continuously. However, most research studies for both imprint technologies have focused on experiments. Few studies have used the numerical method. The transferred pattern will be significantly damaged by a strong adhesion under smaller feature size. Molecular dynamics (MD) simulation is an effective tool for studying material behavior at the nanometer scale as it provides detailed deformation information and the size effect at the atomic level. Nanosystems that have been analyzed using MD include surface friction [6, 7], nanoscratch [8], lubrication [9], nanoimprint [10], contact [11], and nanoindentation behavior [11–13]. Several studies have recently investigated the NIL process using MD. The nanopattern formation and physical mechanism were investigated on metal film imprint by changing the imprint temperature, imprint velocity [14], and stamp taper angle [10, 15]. Kang et al. [16] studied the deformation behavior

on an amorphous polymethylmethacrylate (PMMA) film by changing the stamp aspect ratio. All these studies used MD with a traditional fixed period boundary.

In this study, a movable boundary condition on a gold substrate is proposed to perform a MD simulation of the RNIL process. The objectives of this study are to understand the deformation behavior of imprinted film and the effect of adhesion and friction with changes of the roller tooth geometry, imprint temperature, and imprint depth using MD simulations. Finally, some simulation results for RNIL are compared with those for NIL under the same tooth size to better understand the deformation and physical mechanisms of the two imprint technologies.

## Methodology

Figure 1a shows a RNIL analysis model. The simulation model consists of a tungsten roller and an Au substrate with a movable periodic boundary condition. The roller and the Au substrate consist of a perfect faced-centered cubic (FCC) single crystal. In order to simplify the roller imprint problem, the roller was assumed to be a rigid body rotated around a fixed center with a clockwise angular displacement of 0.002° per time step. The unit of time step was $10^{-15}$ s. The characteristic width and height of the roller tooth were both 8 nm. The roller was composed of 11294 atoms. The width and height of the Au substrate, which was composed of 99840 atoms, were 32.6 and 21.2 nm, respectively. A two-dimensional system was simulated with the surface normal parallel to the *Z*-axis. *X*-, *Y*-, and *Z*-axes are taken in (110), $(\bar{1}00)$, and (101) directions, respectively. A periodic boundary condition was applied to the *X*- and *Y*-axes. Only six unit cells were considered for the periodic boundary on the substrate's *Y*-axis. The periodic boundary on the substrate's *X*-axis was movable in the direction toward the roller. The ratio of the substrate's speed to the roller's tangential speed was 2:3; the speed ratio means the ratio of moving speed of the substrate on *X*-axis to the tangential speed of the roller rotated. The whole boundary size was constant, but the left boundary (LB) and the right boundary (RB) changed with each time step. The new boundaries can be calculated using $LB_{\text{new}} = LB_{\text{ini}} + NS \times U$ and $RB_{\text{new}} = RB_{\text{ini}} + NS \times U$, where the subscript "ini" represents the initial position for a left or a right boundary, *NS* represents the number of time steps, and *U* represents the unit displacement. The value of *U*, which is positive or negative, can be used to determine to the movement direction. Tight-binding many body potential [17] was used to simulate the roller imprint process. The potential form is written in the following, where $E_I^{\text{R}}$ and $E_i^{\text{B}}$ represent a repulsive core interaction and the band energy, respectively, associated with the *i*-th atom:

$$U_{\text{s}} = \sum_i \left(E_i^{\text{R}} + E_i^{\text{B}}\right) \tag{1}$$

where $E_i^{\text{R}}$ is a repulsive pair potential:

$$E_i^{\text{R}} = \sum_{j \neq i} U_{ij}(r_{ij}) \tag{2}$$

$$U_{ij}(r_{ij}) = A \exp\left(-p\left(\frac{r_{ij}}{r_0} - 1\right)\right) \tag{3}$$

and $E_i^{\text{B}}$ represents the cohesive band energy form:

$$E_i^{\text{B}} = -\left(\sum_{j \neq i} \phi(r_{ij})\right)^{\frac{1}{2}} \tag{4}$$

$$\phi(r_{ij}) = \xi^2 \exp\left(-2q\left(\frac{r_{ij}}{r_0} - 1\right)\right) \tag{5}$$

In Eqs. 2–5, $r_{ij}$ is the separation between atoms *i* and *j*, $r_0$ is the first neighbor distance, and *A*, $\xi$, *p*, *q* are adjustable parameters governing the interaction between those atoms. The related parameters are listed in Table 1 [17]. The whole system was put at an isothermal state of 300 K by rescaling the velocities of the atoms [18]. The velocity Verlet algorithm with a time step of 1 fs was used for the time integration of Newton's equations of motion. Figure 1b shows a picture of the roller tooth's taper angle ($\theta$). Five molds with taper angles of 0°, 5°, 10°, 15°, and 20°, respectively, were used in the RNIL process.

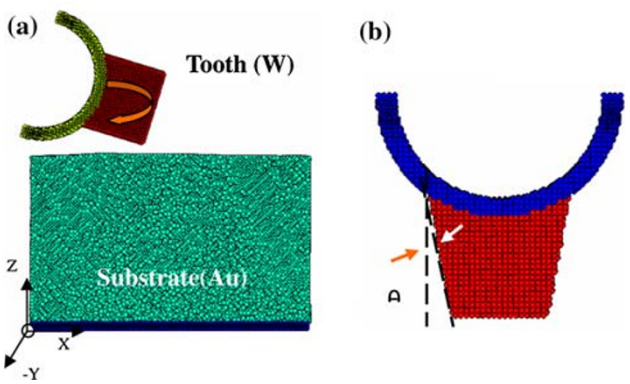


**Fig. 1** Schematic models of **a** rolling imprinting and **b** the tooth's taper angle, $\theta$ (0–20°)

**Table 1** Parameters of tight-binding many body potential [17]

| Element | Parameters | | | | |
|---|---|---|---|---|---|
| | $\xi$ (eV) | *A* (eV) | *p* | *q* | $r_0$ (Å) |
| Au–Au | 1.7581 | 0.1935 | 10.4342 | 3.9472 | 2.8838 |
| Au–W | 2.3739 | 0.2195 | 10.4029 | 2.9694 | 2.8124 |

## Results and Discussion

### Mechanism of Roller Nanoimprint

In order to investigate the deformation behavior and roller imprint force, a MD simulation of imprint was first conducted on the (001) surface of the substrate at room temperature. Snapshots of the roller imprint process are shown in Fig. 2. Here, the rotation angle was 0° when the tooth was located on the right side, the rotation angle was 90° when the tooth was located at the bottom, and the rotation angle was 180° when the tooth was located on the left side. Figure 2a shows that at rotation angle of 49°, a small disturbance occurs at surface atoms close to the tooth that cut into the Au substrate at a specific angle. In the region of Au atoms away from the tooth, a special atomic structure of slip planes of (101) and $(\bar{1}0\bar{1})$ with a cross-like shape was observed. Plastic deformation originated in the slip planes, where the maximum von Misses tension [19] occurs in the substrate [20]. The initial atomic flow characteristic was related to the tooth shape and its relative motion to the substrate. When the rotation angle reached 73°, as shown in Fig. 2b, there were more disorder zones and packed zones around the roller tooth. From a physical point of view, two kinds of mechanical effect occur on the Au substrate. One is the "pushed behavior" that occurs on the substrate atoms that are located on the left side of the roller, and the other is the "pulled behavior" that occurs on the right side of the roller. The "push" and "pull" action contributes to the near-perpendicular atomic flow behavior on the two sides of the pattern. However, in Fig. 2, the pattern shape first appears on the pulled side. In Fig. 2b, the Au surface atoms on the right side of the tooth had little non-continuous flow. When the rotation angle was beyond 90°, the pattern shape gradually appeared as shown in Fig. 2c, d. Interestingly, the forming mechanism occurred on the pulled side because as the pattern formed instantaneously, the bonding force among substrate atoms was larger than the adhesion force between the substrate and the roller atoms. Although the initial pattern shape appeared, a good pattern is still determined by the subsequent adhesion force interaction, as shown in Fig. 2d.

In order to determine the physical mechanism in the roller imprint process, the roller imprint force was varied; the resultant angle ($\alpha$) and the roller rotation angle are shown in Fig. 3. The imprint force in the MD simulation

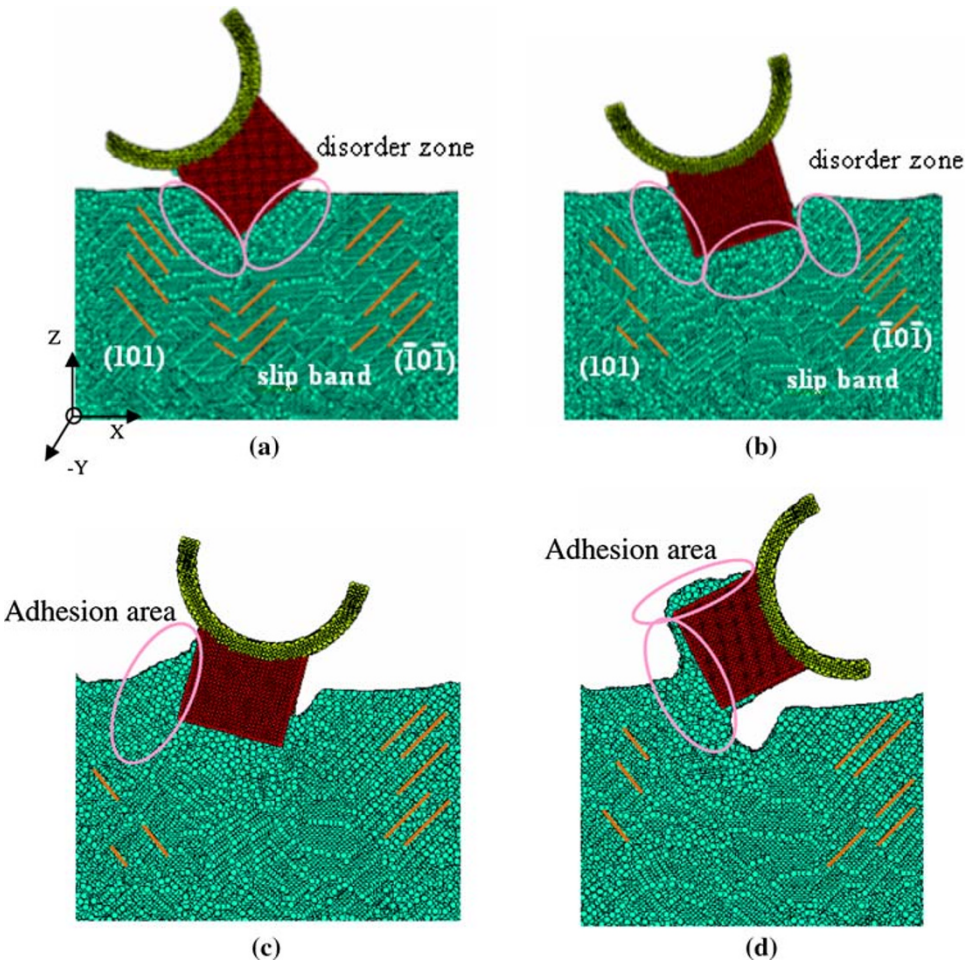


**Fig. 2** Snapshots of rolling imprinting at a temperature of 300 K for rotation angles of **a** 49°, **b** 73°, **c** 105°, and **d** 153°

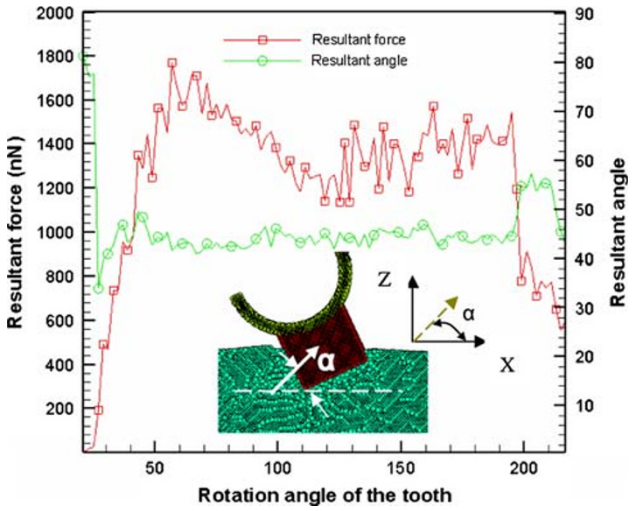


**Fig. 3** Rolling imprint force and resultant angle (α) versus rotation angle diagram

was obtained by summing the atomic forces of the substrate atoms on the X–Z plane of the mold atoms (the *X*-axis is the direction of the substrate movement and the *Z*-axis is the vertical direction). It is a force, not a pressure because the evaluation without considering the action area. The resultant angle was obtained using the sine rule. The force curve distribution indicates that the roller imprint process can be divided into two periods. The first period is the imprint forming stage at rotation angles from 0° to 130°, and the other period is the unloading and adhesion stages at rotation angles was larger than 130°. In the first period of roller imprint, the imprint force increased rapidly as more force was required to deform the single crystal material which had no defects inside. The variation in amplitude of the imprint force is due to the stick–slip phenomena [21]. The input imprint force kept increasing until the rotation angle reached about 58°. In the roller imprint process, this is a critical angle at which the imprint force reaches a maximum value; in this case, this value is 1760 nN. However, this critical angle is not a constant; it changes with the imprint depth. Once the roller rotates past this critical angle, the tooth's body is nearly inserted into the substrate. At this time, the tooth rotates to become almost horizontal. It attaches to the substrate and the input force gradually decreases. The resultant angle variation initially had a high value of about 80°. This indicates that the normal force (in the *Z*-axis) was dominant when the roller and the substrate had just contacted. The resultant angle decreased rapidly after passing the rotation angle of 27°. Then, it maintained a slight oscillation with an average angle of about 45°. The oscillation is related to the stick–slip phenomena. Entering the second period, the imprint force increased again when the rotation angle was higher than 130°. As shown in Fig. 2d, the imprint force increased because of the strong adhesion force between the tooth and the substrate atoms as they pulled to be separated. In this period, the force curve increasingly oscillates. The amplitude indicates the serious extent of the adhesion interaction. The resultant angle had an average value of about 45° in the second period, but this did not agree with our assumption that it should be a negative value when the rotation angle is beyond 90°. This discrepancy can be explained by Fig. 2d. The adhesion occurred on the left side and at the bottom of the tooth during unloading. Therefore, the imprint force and resultant angle were dominated by a strong adhesion force. The force gradually returned to 0 nN and the resultant angle suddenly jumped to about 55°. The jump wascaused by the materials suddenly separating from each other. According to the variance of imprint force and resultant angle, the force during the second period was completely due to adhesion. The resultant angle value indicates the importance of the tooth's strength design.

## Initial Dislocation Nucleation and Interaction on Roller Nanoimprint

Dislocation morphology is important for understanding the fundamental deformation mechanism at the imprint beginning. Dislocation movement is a common mechanism, particularly for metals of sufficient slip systems. In order to clearly display dislocation structures and atoms with high displacement, the slip vector calculation was used to present atomic colors, as shown in Fig. 4. The slip vector shows another kind of strain distribution which was evaluated using the atomic position difference from the initial position to the specified position. The vector on the *i*-th atom can be calculated as:

$$s = \left| r_i^{\text{ini}} - r_i^{\text{spe}} \right| \tag{6}$$

The atoms had a higher magnitude of slip vector, indicating that the amount of displacement was significant. Figure 4a shows that the first load deflection occurred when the rotation angle reached 25° (Fig. 3), which corresponds to the dislocation nucleation near the tooth. Before reaching this rotation angle, the substrate underwent purely elastic deformation since no dislocations were observed. A disorder zone appeared on the surface. After the nucleation, the dislocations extended to the intersection point and formed locks. The dislocation reaction is

$$\frac{1}{6}a[\bar{1}\bar{1}2] + \frac{1}{6}a[\bar{1}\bar{1}\bar{2}] \rightarrow \frac{1}{3}a[\bar{1}\bar{1}0] \tag{7}$$

where $a$ is the lattice constant of Au. The Burger's vector of the lock $\frac{1}{3}a[\bar{1}\bar{1}0]$ is out of the slip plane direction, which is constrained by the quasi-2D simulation. The lock is termed a nominal lock. When the roller's rotation angle

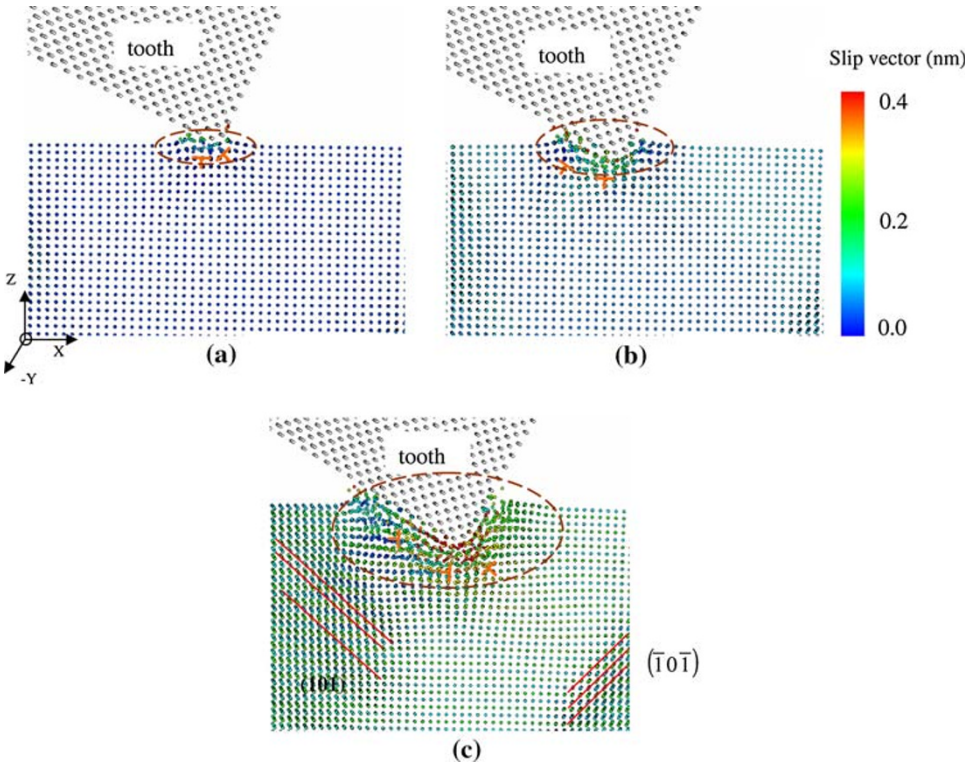


**Fig. 4** Snapshots of rolling imprinting at a temperature of 300 K for rotation angles of **a** 25°, **b** 27°, and **c** 31°. The atomic color is presented by slip vector values

gradually increased as shown in Fig. 4b to an angle of 27°, the disorder and lattice defects zone gradually extended along the tooth shape and the orientation of dislocations became more notably visible. Each dislocation nucleation was accompanied by stress relaxation (load drop). The stress needed to build up again to trigger further activities. Further imprinting caused the slip planes of (101) and $(\bar{1}0\bar{1})$ to occur at the left and right sides of the tooth at a rotation angle of 31°, as shown in Fig. 4c.

## Effect of Taper Angle on Roller Nanoimprint

In addition to the above simulation for tooth geometry with a taper angle of 0° and an imprint depth of 4.5 nm, MD simulations were carried out for four other taper angles to investigate the roller imprint mechanics. The taper angle was changed to 5°, 10°, 15°, and 20°, as shown in Fig. 1b. Figure 5a and b shows imprint forces in the X- and Z-components versus the rotation angle for five taper angles predicted by MD simulations. According to the simulation results, the imprint forces in the X- and Z-components increased more with decreasing taper angle. This occurred because the roller tooth cut into the Au substrate, whose imprint force decreased with the tooth's smoother geometry. The smoothness was proportional to the taper angle. Figure 5 shows that the imprint force obviously decreased when increased only by a few degrees from 0°. The imprint roller with an angle of 15° was the

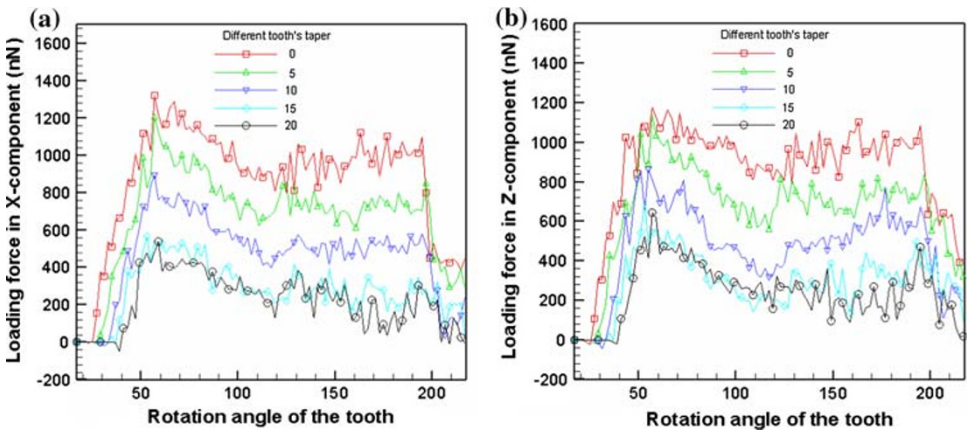


**Fig. 5** Imprint force versus rotation angle diagram at five different taper angles. The force curve is **a** in the X-component and **b** in the Z-component

most suitable. The force curve distributions in Fig. 5 clearly show the two imprint periods. However, the adhesion at the unloading period decreased with increasing taper angle.

*Effect of Imprint Depth on Roller Nanoimprint*

The MD simulations were carried out for four imprint depths to investigate the roller imprint mechanics: 1, 3, 4.5, and 6 nm. Figure 6a, b shows imprint forces in the X- and Z-components versus the rotation angle at the four imprint depths. The maximum imprint force in the loading period increased with imprint depth. The effect of imprint depth was especially strong in the Z-component, as shown in Fig 6b. The time at which the maximum imprint force occurred was inversely proportional to the imprint depth. At an imprint depth of 1 nm, the maximum imprint force occurred near a rotation angle of 90°, the moment when the roller was about to go upward. This indicates that the imprint depth dominates the magnitude of the maximum imprint force and the time when it happens. In the unloading process, the adhesion increased as the imprint depth increased.

Comparison of Mechanisms Between Vertical Imprint and Roller Imprint

In order to better understand the forming mechanism at vertical imprint and roller imprint processes, a special case for vertical imprint was used. For simplicity of comparison, the punch was assumed to have the same size and the same shape as those of the former roller. The motion was set to be in the vertical direction only during the imprint onto the Au substrate. Figure 7 shows the simulation results of imprint force with respect to the punch position for a vertical imprint process. From the force curve of Fig. 7, it can be seen that the imprint process was divided into two periods: the loading period and the unloading period. In the first period, the imprint force increased rapidly with increasing punch position until it reached to a maximum depth of 7 nm. A comparison of the force curve with that for roller imprint in Fig 3 shows that oscillations frequently appeared in the vertical imprint process. This indicates that a regular stick–slip phenomena occurred when the punch maintained a unit displacement while being imprinted onto the Au substrate. The imprint force was not only due to the lateral friction from the side wall and neighboring Au atoms, but also due to the reactive normal force from the bottom Au atoms. According to the simulation, the maximum imprint force in the vertical imprint process was smaller than that of the roller imprint. This result is not in agreement with the results of Ref. [3]. This discrepancy can be attributed to the different imprinted materials and larger pattern size, which were used in the cited reference. After the loading process, the imprint force decreased rapidly from 960 nN to 520 nN. The pattern had already formed and the punch was drawn out gradually. Then, the force curve rose slowly again due to the adhesion interaction with the Au atoms near the pattern walls. Finally, the imprint force stayed at an average of about 780 nN while the punch left the interaction region. At this time, the interaction force still existed because some Au atoms remained attached to the punch tip. A comparison of vertical imprint and roller imprint during the unloading process showed that the latter had larger adhesion and a longer period than the former due to different mold motion characteristics.

The normal stress distribution and slip vector at an imprint depth of 4 nm for the two imprint processes are shown in Figs. 8 and 9, respectively. A different forming mechanism was found in the normal stress distribution in Fig. 8. It can be seen that the high stress value was only concentrated in the region where Au atoms are underneath the punch for a vertical imprint process. The high stress value also existed at deeper layers underneath the punch. For the roller imprint process, the high stress value was

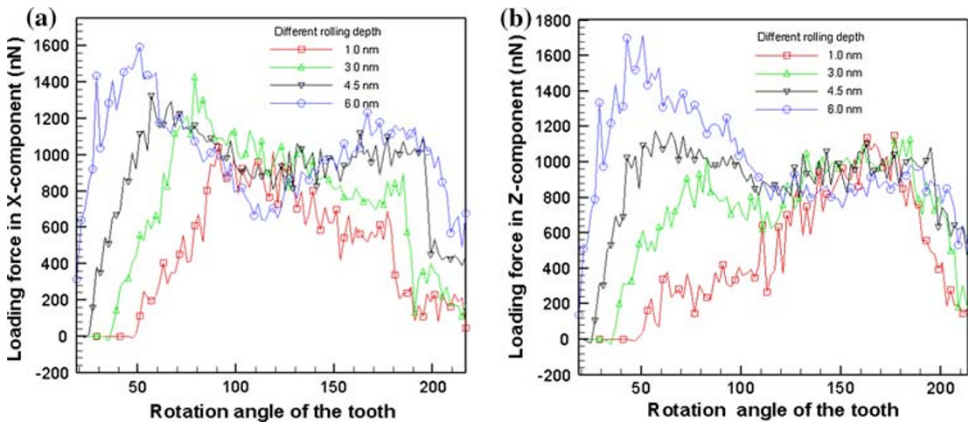


**Fig. 6** Imprint force versus rotation angle diagram at four imprint depths. The force curve is **a** in the X-component and **b** in the Z-component

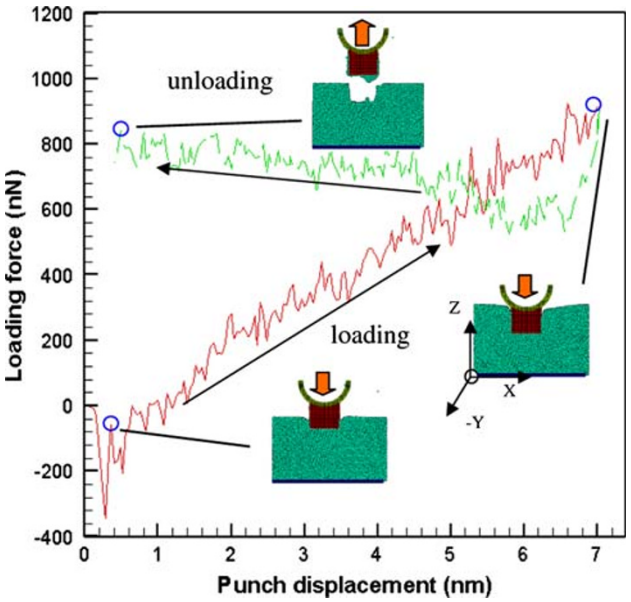


**Fig. 7** Vertical imprint force versus punch displacement diagram

concentrated in the regions where the Au atoms were underneath and around the tooth due to a wide influence scope. The maximum stress value which appeared in the vertical imprint process was smaller than that of roller imprint. Figure 9 shows the slip vector distribution of the imprinted Au substrate. For the vertical imprint process in Fig. 9a, the high slip vector was completely concentrated on the Au atoms underneath the punch. The high slip vector region in the vertical imprint can be called the "dead metal zone" [10]. For the roller imprint in Fig. 9b, the highest slip vector was concentrated on Au atoms underneath the punch; the magnitude decreased with increasing distance from the tooth action radius. There was a minor high slip vector on the Au atoms around the tooth.

Effect of Imprint Temperature on Roller Nanoimprint

In order to observe the effect of temperature on the roller imprint process, three temperature conditions were studied. Figure 9c, d show the slip vector distribution at the imprint temperatures of 400 K and 500 K, respectively. Compared with the room temperature imprint of Fig. 9b, a higher magnitude of the slip vector behavior was found when the temperature increased. The plastic flow increased when the kinetic energies of material atoms increased with increasing temperature. In Fig. 9c, d, the magnitude of the slip vector is proportional to the temperature and its relative distribution scale under the specific temperature is similar. The results indicate that the processes have similar imprint mechanisms and material defaults (the same slip planes). The plastic flow was good so a lower loading force was required when the imprint temperature increased.

## Conclusion

The real material of a roller imprint is a polymer, such as PMMA. The simulations were conducted on gold using the same mold in both nanoimprint and roller imprint processes for convenience and to simplify the comparisons. According to the loading action, some characteristics, such as the distributions of stress, the slip vector, and the effect of the tooth taper, may be similar for the roller imprint on polymers and single crystal metals. As regards the behavior of the vertical imprint process, the amount of extrusion on polymer film [16] was greater than that in metal film [15] when both films underwent loading. The forming discrepancy can be explained by the different interaction forces. Intra- and inter-chain forces are present in the polymer, so the chain molecules have complicated and lenghthy interactions, leading to elongation and entangling between chain molecules. As regards the adhesion effect for polymer imprint, it seemed that the obvious adhesion phenomena were not to be found in snapshots or force curve as were found in Ref. [16]. Those authors found that the contribution of adhesion was small when the PMMA film was imprinted using the Ni mold.

The imprint force, adhesion, stress, and strain distributions of the roller imprint process were studied using MD

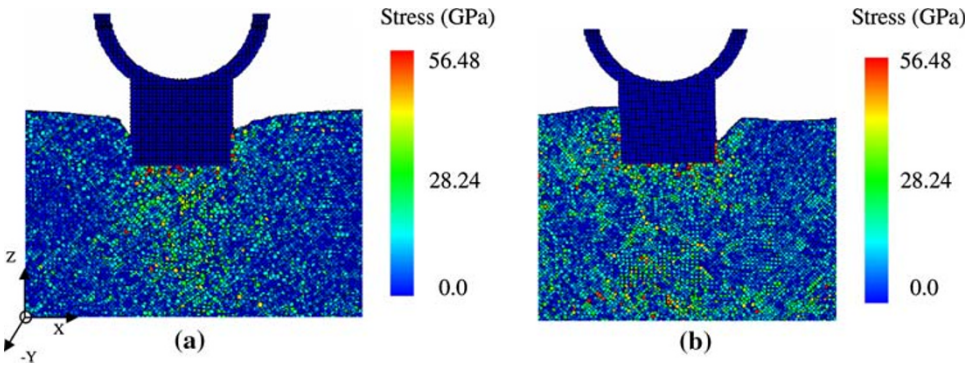


**Fig. 8** Stress distribution in the process of **a** nanoimprinting and **b** roller imprinting

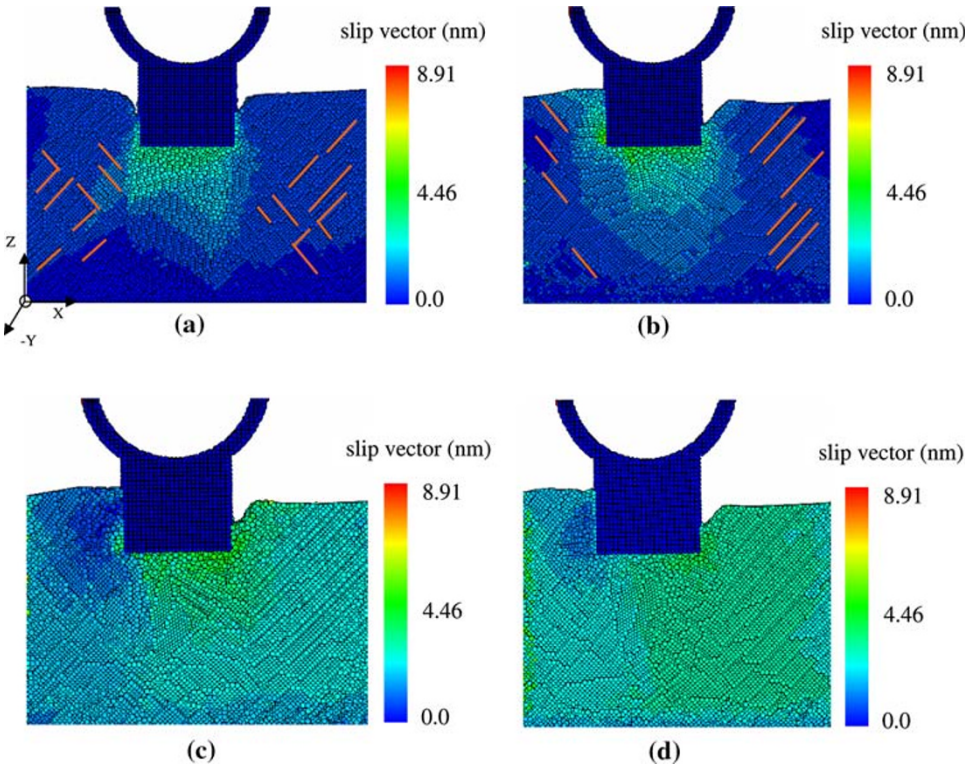


**Fig. 9** Slip vector distribution in the process of nanoimprinting **a** and roller imprinting (**b** and **d**). **a** and **b** were simulated at room temperature and **c** and **d** were simulated at a temperature of 400 K and 500 K, respectively

simulations based on tight-binding many body potential. The results showed that the imprint force and adhesion rapidly increased with decreasing taper angle and increasing imprint depth. The magnitude of the maximum imprint force and the time when it happens were directly proportional to the imprint depth, but independent of the taper angle. A comparison of the imprint mechanisms of the roller imprint and a vertical imprint case showed that the main high stress and strain regions were concentrated on the substrate atoms underneath and around the mold during the roller imprint process whereas these regions were concentrated only on the substrate atoms underneath the mold during the latter process. The plastic flow increased with increasing imprint temperature.

**Acknowledgments** This study was supported in part by the National Science Council of Taiwan under Grant No. NSC95-2221-E150-066.

## References

1. S.Y. Chou, P.R. Krauss, P.J. Renstrom, Appl. Phys. Lett. **67**, 3114 (1995). doi:10.1063/1.114851
2. S.Y. Chou, P.R. Krauss, P.J. Renstrom, Science **272**, 85 (1996). doi:10.1126/science.272.5258.85
3. H. Tan, A. Gilbertson, S.Y. Chou, J. Vac. Sci. Technol. B **16**(6), 3926 (1998). doi:10.1116/1.590438
4. M. Pudas, J. Hagberg, S. Leppävuori, J. Eur. Ceram. Soc. **24**, 2943 (2004). doi:10.1016/j.jeurceramsoc.2003.11.011
5. M. Pudas, J. Hagberg, S. Leppävuori, IEEE Trans. Electron Packag. Manuf. **25**, 335 (2002). doi:10.1109/TEPM.2002.807728
6. M.H. Muser, Comput. Phys. Commun. **146**(1), 54 (2002). doi:10.1016/S0010-4655(02)00434-4
7. R. Komanduri, N. Chandrasekaran, L.M. Raff, Phys. Rev. B **61**(20), 14007 (1997). doi:10.1103/PhysRevB.61.14007
8. T.H. Fang, C.I. Weng, Nanotechnology **11**, 148 (2000). doi:10.1088/0957-4484/11/3/302
9. R. Capozza, A. Fasolino, M. Ferrario, A. Vanossi, Phys. Rev. B **77**, 235432 (2008). doi:10.1103/PhysRevB.77.235432
10. Q.C. Hsu, C.D. Wu, T.H. Fang, Jpn. J. Appl. Phys. **43**(11), 7665 (2004). doi:10.1143/JJAP.43.7665
11. A. Buldum, S. Ciraci, I.P. Batra, Phys. Rev. B **57**(4), 2468 (1998). doi:10.1103/PhysRevB.57.2468
12. T.H. Fang, C.I. Weng, J.G. Chang, Mater. Sci. Eng. A Struct. Mater. Prop. Microstruct. **357**, 7 (2003)
13. C.L. Kelchner, S.J. Plimpton, J.C. Hamilton, Phys. Rev. B **58**(17), 11085 (1998). doi:10.1103/PhysRevB.58.11085
14. Q.C. Hsu, C.D. Wu, T.H. Fang, Comput. Mater. Sci. **34**, 314 (2005). doi:10.1016/j.commatsci.2005.01.004
15. Q.X. Pei, C. Lu, Z.S. Liu, K.Y. Lam, J. Phys. D Appl. Phys. (Berl) **40**, 4928 (2005)
16. J.H. Kang, K.S. Kim, K.W. Kim, Tribol. Lett. **25**(2), 93 (2007). doi:10.1007/s11249-006-9053-4
17. M.A. Karolewski, Radiat. Eff. Defects Solids **153**, 235 (2001). doi:10.1080/10420150108211842
18. J.M. Haile, *Molecular Dynamics Simulation: Elementary Methods* (Wiley, New York, 1992)
19. A. Ganneapali, S.K. Mallapragada, Phys. Rev. B **66**, 104103 (2002). doi:10.1103/PhysRevB.66.104103
20. R.A. Iglesias, E.P.M. Leiva, Acta. Mater. **54**, 2655 (2006). doi:10.1016/j.actamat.2006.02.004
21. T.H. Fang, C.I. Weng, J.G. Chang, Surf. Sci. **501**, 138 (2002). doi:10.1016/S0039-6028(01)01938-0